EPJ manuscript No.
(will be inserted by the editor)

Vortex Washboard Voltage Noise in Type-II Superconductors

Thomas J. Bullard[1,3], Jayajit Das[2], George L. Daquila[1], and Uwe C. Täuber[1]

[1] Department of Physics and Center for Stochastic Processes and Engineering, Virginia Polytechnic Institute and State University, Blacksburg, VA 24061-0435, USA
[2] Department of Chemical Engineering, Massachusetts Institute of Technology, Cambridge, MA 02139, USA
[3] U.S. Air Force, Wright–Patterson Air Force Base, OH 45433-5648, USA

January 20, 2014

Abstract. In order to characterize flux flow through disordered type-II superconductors, we investigate the effects of columnar and point defects on the vortex velocity / voltage power spectrum in the driven non-equilibrium steady state. We employ three-dimensional Metropolis Monte Carlo simulations to measure relevant physical observables including the force-velocity / current-voltage (I-V) characteristics, vortex spatial arrangement and structure factor, and mean flux line radius of gyration. Our simulation results compare well to earlier findings and physical intuition. We focus specifically on the voltage noise power spectra in conjunction with the vortex structure factor in the presence of weak columnar and point pinning centers. We investigate the vortex washboard noise peak and associated higher harmonics, and show that the intensity ratios of the washboard harmonics are determined by the strength of the material defects rather than the type of pins present. Through varying columnar defect lengths and pinning strengths as well as magnetic flux density we further explore the effect of the material defects on vortex transport. It is demonstrated that the radius of gyration displays quantitatively unique features that depend characteristically on the type of material defects present in the sample.

PACS. 74.25.Qt Vortex lattices, flux pinning, flux creep – 74.25.Sv Critical currents – 74.40.+k Fluctuations (noise, chaos, nonequilibrium superconductivity, localization, etc.)

1 Introduction

The physics of interacting vortex lines in high-temperature superconductors subject to strong thermal fluctuations and pointlike or extended disorder is amazingly rich and has been a major research focus in condensed matter physics in the past two decades [1]. Vortex motion plays a crucial role in the transport properties of type-II superconductors in external magnetic fields. In the presence of a sufficiently large applied current magnetic flux lines will experience a Lorentz force and drift perpendicular to both the current and applied magnetic field. The motion of these current-encircled magnetic flux filaments induces an electric field parallel to the applied current resulting in power dissipation and hence an Ohmic voltage drop across the material proportional to the velocity of the vortices. While an externally applied current serves as a driving force, underlying defects in the superconducting material inhibit vortex motion. Material defects pin vortices below a critical applied force, and also play a significant role in their motion above that threshold, providing, on a coarse-grained description level, an effective friction or viscosity.

Aside from the obvious relevance for technological applications, driven magnetic flux lines in type-II superconductors also represent one of the few cleanly experimentally realizable systems of interacting particles in a non-trivial non-equilibrium steady state. A thorough understanding of the ensuing phase diagram and full characterization of each emerging steady state should shed light on the rich and still rather incompletely understood features of non-equilibrium systems in general. Since stochastic fluctuations and intrinsic correlations typically play a significant role away from thermal equilibrium, it is desirable for each emerging stationary state to attain a thorough quantitative understanding of the fluctuations.

In superconductors specifically, pinning effects on vortex motion are also reflected in the voltage noise power spectrum [2]. For instance, slightly above the critical force, in the presence of strong disor-

der, depinning of vortices is observed to proceed via flow through plastic channels [3]. These 'rivers' of vortices form at different locations in the sample, and flow around 'islands' of temporarily trapped flux lines resulting in incoherent motion. Such behavior has been observed experimentally [4], as well as in two-dimensional computer simulations [5], and is characterized in the velocity or voltage frequency power spectrum by a broadband noise signal which obeys a $1/\omega^{\alpha}$ power law, as also demonstrated in recent three-dimensional numerical work [6].

Well above the critical force it has been observed that vortices are more translationally ordered than at low velocities [7]. It might be expected that at a sufficiently high drive, the vortices would form a moving Abrikosov lattice since the effective pinning force from the disorder on each vortex varies rapidly and would therefore be less effective [8]. However, it has been shown by Le Doussal and Giamarchi [9] that some modes of the disorder are not affected by the motion even at large velocities. As a result the vortices enter what has been termed a 'moving glass' phase. Here, subtle competitions between elastic energy, disorder, and dissipation lead to the transverse displacements becoming pinned into preferred time-independent configurations resulting in stationary two-dimensional channels. In the moving glass phase, vortices thus follow each other in a manner similar to beads on a wire.

There exist a few possible coupling regimes between these elastic channels. For strong point disorder approximately parallel elastic channels are completely decoupled, while the periodicity along the direction transverse to the drive is maintained. Here sharp delta-function Bragg peaks with nonzero reciprocal-lattice vector components along the direction of motion are lost, while peaks with only transverse components remain. This regime is known as the 'moving transverse glass' or 'moving smectic' phase [9], and is supported by recent numerical simulations in two and three dimensions [10,11]. On the other hand, for weak point disorder, or large velocities, relative deformations grow only logarithmically with distance; hence, the vortex structure maintains quasi long-range order corresponding to complete elastic coupling between vortices. This state is known as a 'moving Bragg glass' and is characterized by algebraically divergent structure factor peaks at small reciprocal lattice vectors [9].

The interaction of the moving Bragg glass with the underlying material defects is manifested by a characteristic peak in the power spectrum corresponding to the periodicity of the vortex lattice [9]. Defects in the material temporarily slow vortices resulting in 'stick-slip' motion. In a structurally ordered phase such as the moving Bragg glass, this behavior is repeated, resulting in a periodically varying average overall velocity. With the lattice vector of the Bragg glass oriented in the flow direction, the resulting characteristic frequency associated with this motion is known as the 'washboard' frequency. Related phenomena are certainly not unique to driven flux lines in type-II superconductors, but are, for example, well-established in charge- and spin-density wave systems [12].

Random point disorder need not be the only pinning structure in superconducting materials. Columnar disorder may also be introduced into materials for the purpose of increasing the critical current [13]. Far above the depinning threshold a 'moving Bose glass' is formed in the presence of columnar pins [9]. Owing to the correlated nature of the disorder along the length of each vortex, the structure function tends to resemble that of the moving transverse glass. Furthermore, akin to the equilibrium Bose glass (i.e., the disorder-dominated amorphous structure formed by flux lines localized by correlated defects [14]), the moving Bose glass displays a diverging tilt modulus [9,15]. Whether a unique voltage noise signal exists for this phase (as well as for the moving transverse glass) is unclear, and subject to this present investigation.

The washboard frequency has been observed in a number of experiments [16,17,18]. However, direct observation of the washboard noise was achieved by Togawa *et al.* [19], who obtained voltage noise spectra of BSCCO crystals in the mixed state subject to a constant current for various applied magnetic field strengths. For low magnetic fields broadband noise was observed and attributed to plastic vortex flow. As the applied magnetic field was increased, the broadband noise signal reached a maximum value and then decreased again, while a narrowband noise peak that corresponded to the washboard frequency emerged. Upon increasing the magnetic field further, the characteristic frequency of the narrowband noise grew owing to a tighter flux line packing of the vortices, and hence a shorter vortex lattice constant. The narrowband noise signal also decreased in height and increased in width. The reason for this is apparently still not fully understood.

Washboard noise has also been detected unambiguously in a number of two-dimensional numerical simulations; as characteristic examples, we mention the following: Olson *et al.* [20] performed molecular dynamics simulations of vortices that were driven through a system of randomly placed defects. Upon varying the drive strength they noticed that the number of regimes available to the system above the plastic flow phase depended on the vortex interaction strength. For systems with intermediate to high interaction strength and large applied drive, the vortices entered a coupled channel regime indicated by sixfold coordination of the structure. In this regime washboard noise was observed. Furthermore, it was noted that the washboard signal intensity decreased as the system size was increased. It is believed that this was due to multiple domains

forming in the vortex lattice resulting in decoherence of the noise signal.

Kolton *et al.* [21] also performed two-dimensional molecular dynamics simulations to investigate Fiory steps [16] for different vortex velocities. In order to understand the relationship between these steps and the temporal order in the different regimes, the voltage power spectrum was investigated without an applied ac drive. The authors observed the evolution of the power spectrum from broadband noise to the emergence of a narrowband peak as the applied dc drive was increased, and also found higher harmonics. Two-dimensional computer simulations employing Langevin dynamics and varying drive and pinning strength have been performed as well [22], with similar washboard noise results.

In contrast, we are aware of only one three-dimensional investigation of the washboard noise. Using an anisotropic XY model Chen and Hu [11] investigated the first-order transition from the moving Bragg glass to the moving smectic. In the moving Bragg glass phase narrowband noise that corresponded to the washboard frequency was observed along with harmonics for various driving strengths at zero temperature. The washboard peak itself persisted for $T > 0$, while its harmonics disappeared. The authors also found that the moving Bragg glass turned into a moving liquid at high drive, and hence that the washboard signal was destroyed. They argue this to be due to thermally activated vortex loops inducing dislocations in the Bragg glass [11].

The purpose of this work [23] is threefold. First, we wish to establish confidence in our novel simulation approach to modeling vortex motion by qualitatively comparing our results to well-known superconducting vortex behavior. Second, we wish to investigate the evolution of the narrowband noise associated with the washboard frequency for increasing vortex density (i.e., increasing magnetic flux density) in the presence of randomly distributed point as well as columnar defects. Finally, we are interested in studying the effects of different types of pinning centers on the narrowband voltage noise. Below the critical current, in the presence of columnar defects, it has been predicted that vortices hop between pinning sites temporarily trading elastic deformation energy in the form of double-kinks and half-loops for a lower overall energy configuration [14]. Well above the depinning current remnants of these half-loop excitations and double kinks may still exist. At high driving values these remnant excitations would occur predominantly in the direction of the drive, while other excitations would be suppressed by the localizing effect of the columnar pins. Obviously, the impact of such vortex excitations on the power spectrum cannot be addressed by a two-dimensional simulation, but require a full three-dimensional model.

Based on the effective free energy for interacting magnetic flux lines in the London approximation, and subject to attractive pinning centers [14], we have developed a three-dimensional Monte Carlo simulation code [24] to study the effects of disorder on the velocity / voltage power spectrum and the two-dimensional static vortex structure factor in the plane transverse to the magnetic field for driven vortices in the non-equilibrium steady state. Specifically, we compare results for point and columnar defects. We also measure the average radius of gyration in order to examine the effects of the different defect types on the shape or thermal 'wandering' of the elastic flux lines along the magnetic field (z) direction. The simulation results reported here should be contrasted with our earlier findings for non-interacting flux lines in the presence of various disorder distributions [24].

Our results display many similar features for both defect types. As the vortex density is increased for systems with either weak point or correlated disorder, positional ordering is observed to increase in the structure factor plot. For columnar defects the vortex structure factor is found to change from that characteristic of a typical liquid, to a smectic, and eventually an ordered triangular lattice. For the case of point defects, we only observe the triangular array in the parameter region studied here. We find that the structure factor plots at low vortex densities in the presence of point disorder appear qualitatively similar to the results for columnar defects at higher densities. As the structure factor begins to display positional order in the direction of the drive a narrowband noise signal in the velocity noise power spectrum corresponding to the washboard effect is detected for both defect types. Associated with the washboard peak are harmonics, the ratios of which initially appear to be related to the type of pinning defect in the system. We present results that suggest these harmonic ratios are in fact not dependent on the type of pinning centers present in the sample.

To further examine these potentially distinct effects on the velocity or voltage power spectrum, we vary the effectiveness of the pinning centers. For a fixed vortex density the positional arrangement of the pinning sites in the system is changed from randomly distributed (i.e., point-like defects) to correlated along the z axis (i.e., columnar defects). The velocity fluctuation power spectra as well as the structure factor plots are examined for this series of simulations as well. We then compare our findings to the results obtained with increasing point defect pinning strength. We find that whereas the power spectrum and structure factor evolve in a qualitatively similar manner when varying the 'pinning effectiveness' through either method, there appear marked differences in the behavior of the mean radius of gyration. Namely, as the point pinning

strength increases, vortices tend to stretch and deform following a $r_g \propto U^2$ behavior, where U represents the pinning potential depth. In contrast, we observe the radius of gyration to saturate for increasing columnar defect length. The behavior is best described phenomenologically as $r_g \propto e^{-l_0/l}$ where l denotes the length of the columnar defects (and l_0 gives the length scale in z direction).

In the following section 2, we describe our model and the simulation algorithm in detail. Section 3 contains our simulation results, as already summarized above. Finally, in section 4, we conclude and provide an outlook for further investigations.

2 Model Description and Simulation Algorithm

In our Monte Carlo simulations, vortices are considered in the London approximation (with the London penetration depth large compared to the coherence length, $\lambda \gg \xi$) as discretized elastic lines [14] (see also Refs. [25,26]). The elastic energy associated with the line tension of N_v flux lines is taken to be

$$E_L = \frac{\epsilon_1}{2} \sum_{i=1}^{N_v} \int_0^L dz \left| \frac{d\boldsymbol{r}_i(z)}{dz} \right|^2 , \qquad (2.1)$$

where $\boldsymbol{r}_i(z)$ describes the configuration of the ith vortex by specifying its two-dimensional position $\boldsymbol{r}$ as function of the coordinate z ($0 \le z \le L$) along the magnetic field direction. The line stiffness is given by $\epsilon_1 = \epsilon_0 \ln\bigl(\xi_{ab}/\lambda_{ab}\bigr)\Gamma^{-2}$, where λ_{ab} is the in-plane London penetration depth, and ξ_{ab} the in-plane superconducting coherence length. $\epsilon_0 = \bigl(\phi_0/4\pi\lambda_{ab}\bigr)^2$ sets the overall energy scale, and $\phi_0 = hc/2e$ is the magnetic flux quantum. The expression (2.1) for the elastic energy holds if $\bigl|d\boldsymbol{r}_i(z)/dz\bigr|^2 \ll \Gamma^{-1}$, where $\Gamma^2 = M_z/M_\perp$ denotes the effective mass ratio for the elastic line. In this study we model high-T_c materials for which $\Gamma \gg 1$. In the simulation each flux line is represented by N_p points located at $(\boldsymbol{r}_i, z_i)$. Each point is confined to a constant z_i (a separate ab plane) and interacts with its nearest neighbors above and below via a simple harmonic potential.

The total interaction energy between all pairs of distinct vortices is

$$E_{\rm int} = \sum_{i \neq j}^{N_v} \int_0^L V\Bigl(|\boldsymbol{r}_i(z) - \boldsymbol{r}_j(z)|\Bigr)\, dz\,, \qquad (2.2)$$

with the pair potential $V(r) = 2\epsilon_0 K_0(r/\lambda_{ab})$. Here, K_0 is the modified Bessel function of zeroth order, and can be described qualitatively as diverging logarithmically as $r \to 0$ and decreasing exponentially for long distances $r \gg \lambda_{ab}$. Interactions between vortices occur only within the ab planes (i.e., consistent with the London limit we neglect any cross-plane interactions); this approximation is valid as long as the requirements for Eq. (2.1) are satisfied. For the simulation, we consider a system of extension L_x and L_y in the x and y directions with periodic boundary conditions. For each vortex pair, we compute its minimal distance within this rectangle and its periodic images adjacent to it, and use that distance to evaluate the interaction potential. As a consequence of this nearest-image approximation, the interaction potential is cut off at distance $\min(L_x/2, L_y/2)$. To minimize the effects of the cut-off, λ_{ab} has been decreased to prevent numerical artifacts observed in the simulation [27]. We have also run Monte Carlo simulations for a cutoff length twice the original length used in the bulk of this study. To accommodate the increase in length the system area was increased by a factor of four. For the larger system the washboard noise is recovered for both columnar and point defects, and higher harmonics are observed for point defects.

Material defects in the system are represented by a distribution of cylindrical potential wells,

$$E_D = \sum_{j=1}^{N_v} \int_0^L V_D\Bigl(\boldsymbol{r}_j(z)\Bigr)\, dz\,, \qquad (2.3)$$

with $V_D\Bigl(\boldsymbol{r}_j(z)\Bigr) = \sum_{k=1}^{N_D} U\Theta\Bigl(b_0 - |\boldsymbol{r}_j(z) - \boldsymbol{r}_k^{(p)}|\Bigr)$. Here b_0 is the pin radius in the ab plane, Θ denotes the Heaviside step function, $\boldsymbol{r}_k^{(p)}$ indicates the location of the kth pinning center, and U characterizes the well depth.

Finally, in the presence of an external current the flux lines experience a force per unit length $\boldsymbol{f}_L = \phi_0 \hat{z} \times \boldsymbol{J}/c$, therefore a corresponding work term is introduced:

$$W = -\sum_{i=1}^{N_v} \int_0^L \boldsymbol{f}_L \cdot \boldsymbol{r}_i(z)\, dz\,. \qquad (2.4)$$

This work contribution favors vortex motion along the direction of the force while suppressing motion against it. For this investigation, the force is always applied in the x direction. The total energy of the system reads $E_{\rm tot} = E_L + E_{\rm int} + E_D + W$.

In our simulations the applied magnetic field is taken parallel to the c axis (oriented parallel to $\hat{z}$); therefore, at time $t = 0$ straight lines are placed vertically in a system of size $L_x \times L_y \times L_z$ with periodic boundary conditions in all directions. We have found that the initial configurations of the individual lines do not affect the steady state attained at long times. Defect centers at positions $\boldsymbol{r}_k^{(p)}$ are also distributed throughout the system, either randomly or aligned parallel to the c axis to model columnar pins. The state of the system is then updated according to standard Monte Carlo Metropolis rates.

When the number of attempted updates is equal to the number of points that make up a flux line multiplied by the total number of lines in the system, this constitutes a single Monte Carlo step (MCS) and serves as the unit of time in the simulation. While this 'driven diffusive system' simulation approach, introduced by Katz, Lebowitz, and Spohn [28], is likely best suited to model thermally activated motion close to equilibrium, we find that our results in the driven regime, considerably away from equilibrium, are quite similar to those observed in other studies, as mentioned above.

Nevertheless, it is not at all obvious even for steady states far from thermal equilibrium which choices of 'microscopic' Monte Carlo rates yield the most 'realistic' representations of an experimental system, even in a coarse-grained view. Gotcheva *et al.* [10] have recently brought into question the general validity of the driven diffusive Metropolis Monte Carlo dynamical method in their simulations for vortices on a two-dimensional lattice. The non-equilibrium steady states obtained using Metropolis Monte Carlo and continuous-time Monte Carlo dynamical rules, respectively, were compared as a function of temperature and driving force. The results differed dramatically depending on which dynamical rule was used. In some instances at least, the Metropolis algorithm yielded a spatially disordered moving steady state while the continuous-time Monte Carlo rules preserved positional order (in finite-size systems) over much of the non-equilibrium phase diagram. The authors argue convincingly that the lack of order observed in the Metropolis simulation was due to intrinsic randomness in the updating rules. It would certainly be interesting and worthwhile to probe to what extent these findings also apply to three-dimensional off-lattice simulations, which are presumably less likely to be stuck in long-lived metastable configurations. In our current study we find that spatial order survives in the non-equilibrium steady state for an extended range of flux density values.

Quite generally, it is crucial for the analysis of out-of-equilibrium systems to carefully investigate alternative approaches to the description of their dynamics in order to probe their actual physical properties rather than spurious artifacts inherent in any mathematical modeling. Different mathematical and numerical representations of non-equilibrium systems in fact rely on various underlying *a-priori* assumptions that must be tested *a-posteriori* by comparing their respective results. For example, many computer simulation studies of driven flux line systems invoke stochastic Langevin equations, wherein one assumes that all fast degrees of freedom are aptly captured in terms of uncorrelated white noise (see, e.g., Refs. [20,29,22]). Such a mesoscopic representation of the dynamics is usually adequate in thermal equilibrium where the form of the input noise correlations is severely restricted by fluctuation-dissipation relations. Yet the large-scale and long-time properties of nonlinear Langevin stochastic differential equations away from thermal equilibrium are well-known to be often drastically affected by the functional form or even strength of the assumed noise correlations, which are not uniquely determined by Einstein relations any more. One would, e.g., suspect that the flux line correlations along the magnetic field axis should be reflected in the noise spectrum and relaxational features. It is therefore imperative to test a variety of different numerical methods and compare the ensuing results in order to identify those properties that are generic to the physical system under investigation.

The parameter values used in our simulations correspond to typical high-T_c materials, and are reported in units of b_0 (the pin radius) and interaction energy scale ϵ_0. The parameters ξ_{ab}, ϵ_1, and Γ^2 are chosen to be $0.5\,b_0$, $0.25\,\epsilon_0$, and 16, respectively. In this study we examine vortex motion in the weak pinning regime. The pinning potential U has been given a value of $U_0 = 0.03125\,\epsilon_0$ while the predicted value is approximately $0.5\,\epsilon_0$ [14]. The penetration depth λ_{ab} is assigned a value of $16\,b_0$ which is about $1/3$ of typical high-T_c values. As previously mentioned this choice was made in order to minimize artifacts due to the interaction cut-off. The average separation distance between randomly distributed defects in each ab plane is taken to be $15\,b_0$. The maximum distance for a point on any flux line to move is limited to $b_0/2$, to help avoid vortices 'hopping' over defects. We have used a discretization along the field direction of $L_z = 20$ parallel planes.

As is well-known in finite-size vortex simulations, a square planar geometry favors ordering into a square lattice whose configurational energy is only slightly above that of the triangular Abrikosov lattice [30]. We have thus chosen the system's planar aspect ratio as $L_x : L_y = 2 : \sqrt{3}$ in order to easily accommodate a triangular lattice. The vortices are then placed in the system prearranged in a triangular array with a lattice vector oriented along the x-direction. Choosing this aspect ratio allows an even square number of vortices to 'fit' in the system while arranged in this configuration. In the simulation runs, the vortex lattice arranged in local energy minima configurations by either aligning a lattice vector parallel to the system's horizontal axis, rotating the lattice vector by 30° from the horizontal, or by arranging such that the lattice twisted about the system at a chiral angle satisfying periodic boundary conditions. When in our simulations an external force is applied and the vortex system driven, we find that the lattice maintains its initial orientation. However, by approximately doubling the defect pinning strength the lattice reorients such that the principal lattice vector points in the direction of the applied drive. Drive-induced

reorientation has been observed in experiments [31] and simulations [22].

Since the present study is primarily concerned with the effect of defect correlations on the dynamics, the temperature is chosen such that $T/T^* < 1$, where $T^* = k_B^{-1}\sqrt{\epsilon_1 U_0}b_0$ is the temperature above which entropic corrections due to thermal fluctuations become relevant for pinned flux lines [14]. Here, thermally induced stretching and wandering of the flux lines are largely suppressed (as long as the vortices remain pinned), and the results can be interpreted in terms of low-temperature kinetics. Our simulations are thus usually run at $k_{\rm B}T$ per unit length equal to $0.004\,\epsilon_0$. The average or center of mass (CM) velocity for each vortex is then calculated and averaged over all vortices:

$$\boldsymbol{v}_{\rm cm} = \frac{1}{N_v}\sum_{i=1}^{N_v}\frac{\boldsymbol{r}_{{\rm cm}_{\rm i}}(t+\tau)-\boldsymbol{r}_{{\rm cm}_{\rm i}}(t)}{\tau}\,, \qquad (2.5)$$

where $\boldsymbol{r}_{{\rm cm}_{\rm i}}$ denotes the center-of-mass position of the ith vortex, and τ is the time interval between measurements. τ is set to 30 MCS, and the simulation is then run for 10^5 MCS to arrive at a steady state. Data are subsequently collected for the next 2.5×10^5 MCS.

From the collected data, we obtain the two-dimensional static structure factor in the plane transverse to the magnetic field,

$$S(\mathbf{k}) = \int \langle\rho(\mathbf{0})\rho(\mathbf{r})\rangle\, e^{-i\mathbf{k}\cdot\mathbf{r}}\, d\mathbf{r}\,, \qquad (2.6)$$

where $\langle\rho(\mathbf{0})\rho(\mathbf{r})\rangle$ denotes the density-density correlation function, for the driven vortices in the nonequilibrium steady state. We also measure the average radius of gyration,

$$r_g = \left(\frac{1}{N_v L}\sum_{i=1}^{N_v}\int_0^L [r_{{\rm cm}_i} - r_i(z)]^2\, dz\right)^{1/2}\,, \qquad (2.7)$$

in order to examine the effects of the different defect types on the shape or thermal 'wandering' of the elastic flux lines along the magnetic field (z) direction. Additional information about the detailed dynamics is encoded in the velocity fluctuation power spectra

$$S(\omega) = \left|\int v(t)\, e^{i\omega t}\, dt\right|^2. \qquad (2.8)$$

These velocity power spectra have been appropriately windowed in order to minimize spectral leakage. Since vortex motion across the sample induces a voltage drop, the velocity fluctuations are experimentally directly accessible as the measured voltage noise. Each of the above observables is measured for various vortex densities and defect configurations. Vortex densities are reported as a count of the number of vortices in a unit system of area $A = 150\frac{2}{\sqrt{3}}\,b_0 \times 150\,b_0$. The vortex structure factor and velocity noise plots are averaged over time and typically over 40-50 disorder realizations.

3 Monte Carlo Simulation Results

3.1 Current-Voltage (I-V) Characteristics

In order to validate our model and simulation algorithm we have examined the average vortex velocity as a function of the applied force and compared our results to well-established experimental and numerical findings. In experiments, the driving force is proportional to the externally applied current, and the induced voltage across the sample proportional to the mean flux line velocity, hence the current-voltage (I-V) characteristics are given by the force-velocity curves in our simulations.

Our simulation results for systems with randomly distributed columnar pins and point defects are plotted for various flux densities in Fig. 3.1. In addition to averaging over all flux lines in the system, the data are averaged over time (25,000 Monte Carlo steps) and five disorder realizations. For both graphs the number of effective pinning sites is equal, as are the pinning strengths (per unit length) U_0 for all the defects.

The vortices are seen to remain pinned for both columnar and point defects up to a critical depinning force, beyond which the system takes on an average velocity that increases with increasing applied drive. As expected the depinning threshold is higher for columnar defects [Fig. 3.1(a)] since the attractive force from each pinning site adds coherently over the length of the flux line. The inset in Fig. 3.1(b) depicts the region of the curve associated with depinning for point defects, showing just the data for the densest and most dilute systems. We observe (again as expected) that denser vortices depin at lower driving currents for either type of pinning center; estimates for the depinning current for columnar defects as obtained from our data are depicted in Fig. 3.1(c). As the repulsive interactions between neighboring vortices grow with flux density, this helps the vortices to overcome the defect pinning potentials. We find that these results are qualitatively comparable to experimental findings in high-temperature superconducting materials (see, e.g., Refs. [32,33,34]), and in accord with results obtained by means of Langevin molecular dynamics simulations [35] (in the three-dimensional regime, see also Ref. [36]), giving us confidence in the validity of our model and algorithm.

However, we note two artifacts in the I-V results occuring at higher driving current and large vortex densities. First, while at large currents linear Ohmic behavior should ensue, we find that the velocity values saturate at high applied drive values,

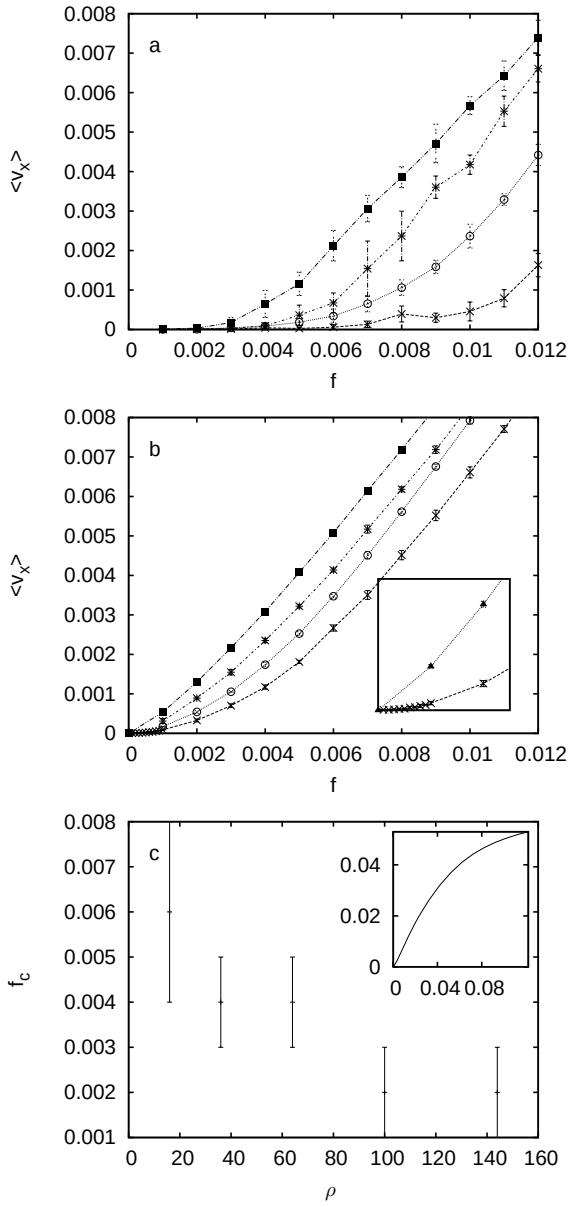

Fig. 3.1. Velocity (induced voltage) vs. force (applied current) curves (I-V characteristics) for (a) randomly distributed columnar pins, and (b) point defects. For both defect types the depinning threshold decreases with increasing vortex / flux density. This can be seen most clearly for point defects in the inset in (b), which amplifies the low current regime: here, the force values on the x axis of the inset range from 0 to 0.0025, the velocity ranges from 0 to 0.0016 and is given in units of b_0/ MCS (pin radius per Monte Carlo step). The following symbols represent vortex densities reported as the areal density ρ in a fixed area $A = 150\frac{2}{\sqrt{3}}\,b_0 \times 150\,b_0$: ▲ $-\ 144/A = 0.00554/b_0^2$, ■ $-\ 100/A = 0.00385/b_0^2$, $*$ $-\ 64/A = 0.00246/b_0^2$, ◯ $-\ 36/A = 0.00139/b_0^2$, $\times$ $-\ 16/A = 0.00062/b_0^2$. (c) Estimate of the depinning force f_c as function of the vortex density ρ for random columnar defects. The inset depicts how the I-V curve for $\rho = 144/A$ saturates at high drive values. In all plots, the data points are connected as a guide for the eye.

see inset of Fig. 3.1(c). This is due to a maximal step size limitation imposed to avoid vortices 'hopping' over pinning defects in the system. Second, the I-V curves are observed to cross at larger densities due to the fact that the system is updated locally rather than globally, in the Metropolis algorithm. At higher vortex densities larger local moves are suppressed by the repulsive potential of nearest neighbors resulting in a lower average velocity and an I-V curve with a lower slope than that of lower density systems.

In the following, we mostly report data that have been collected at a driving force $f = 0.04$. This high value was chosen so that washboard noise could be observed over a range of accessible vortex densities; however, in some instances the I-V curve has already begun to saturate. Since we are studying the velocity noise spectrum relative to the mean velocity, we do not expect specific artifacts caused by the saturation in the voltage noise, nor do we observe any as compared to results obtained at lower drive values $f = 0.01$ (see the discussion at the end of Sec. 3.2.1).

3.2 Narrowband Noise Characteristics

Power spectral density plots and intensity plots of the structure factor $S(\mathbf{k})$ have been obtained for several vortex densities as shown in Figs. 3.3 and 3.8. Unless otherwise indicated, all power spectral density plots are double-logarithmic with the frequency on the x axis ranging from 0.001 to 0.1 rad / MCS and power in normalized units on the the y axis in the range $2.5 \times 10^{-10} \ldots 1 \times 10^{-4}$. Distinct peaks are observed as well as higher harmonics in many of the power spectra for columnar defects. Peaks are observed in all of the power spectral plots for point defects. In both cases harmonics are always located at integer multiples of the fundamental frequency. In Fig. 3.2 the fundamental frequencies are plotted versus the number of vortices per unit system size along with the predicted washboard frequencies for both point and columnar disorder. The washboard frequency is calculated by simply dividing the measured average vortex velocity $\langle v_x \rangle$ (parallel to the applied drive, and averaged over time and defect realizations) by the vortex triangular lattice constant. Due to the aspect ratio of the system this distance is obtained by dividing the system length in the direction of the drive (L_x) by the square root of the number of vortices in the system; hence,

$$\omega = 2\pi \langle v_x \rangle \sqrt{N_v}/L_x. \tag{3.1}$$

We obtain good agreement between the measured and predicted values indicating that the fundamental frequency in the power spectra plots is indeed the washboard frequency. Error bars for the measured frequencies are estimated by taking the full

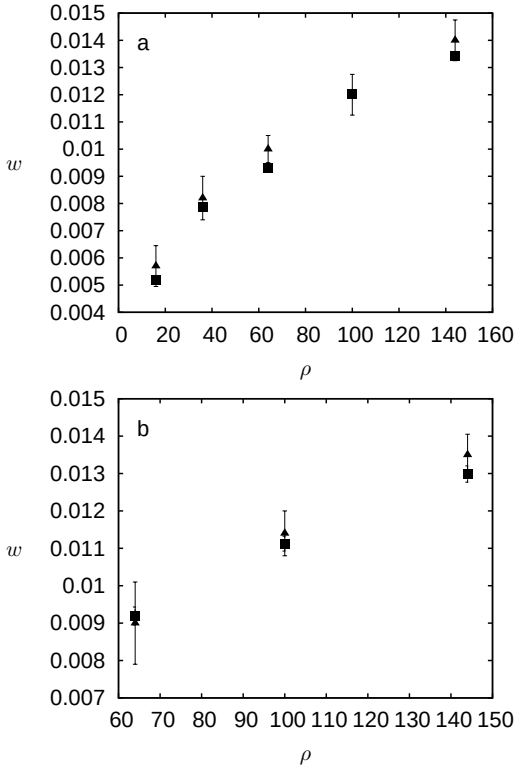

Fig. 3.2. Washboard frequency versus vortex density ρ for (a) point and (b) columnar pinning centers. Vortex density is reported as a count of the number of flux lines in a fixed area of size $A = 150\frac{2}{\sqrt{3}}\,b_0 \times 150\,b_0$. The results show good agreement between the measured and calculated values for both defect types. The frequency ω is given in units of rad / MCS. Error bars for the measured values are obtained from the full width at half-maximum of the washboard peaks in Figs. 3.3 and 3.8. Error bars for the calculated values are smaller than the data points. ▲ - measured, ■ - calculated.

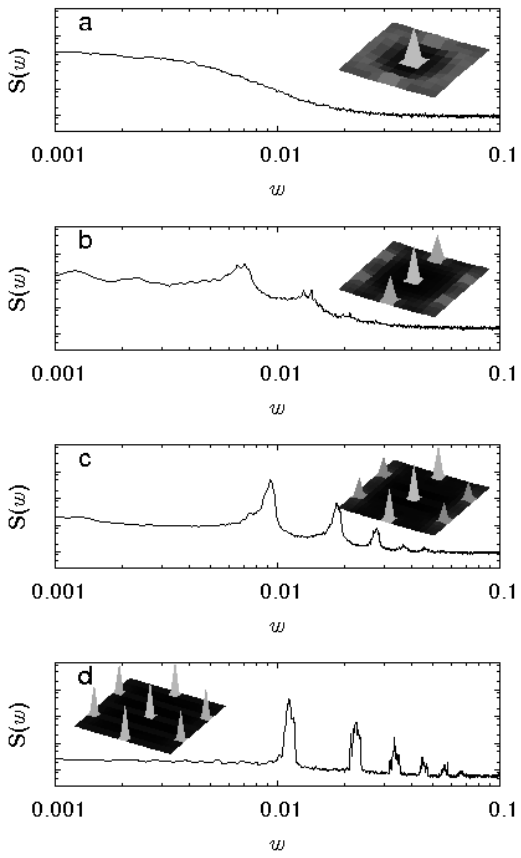

Fig. 3.3. Velocity / voltage power spectra measured in the direction of the drive (x direction) and structure factor plots for increasing vortex density in the presence of randomly distributed columnar defects. (a) For a density $\rho = 16/A = 0.00062/b_0^2$ an isotropic liquid is observed along with a broadband noise signal in the power spectrum. (b) At $\rho = 36/A = 0.00139/b_0^2$ two (off-center) peaks appear in the structure factor located transverse to the drive direction, accompanied by a narrowband signal in the velocity power spectrum. (c) Six peaks appear in the structure factor plot for $\rho = 64/A = 0.00246/b_0^2$. The intensities of the peaks with a wave vector component in the x direction are lower than those with only a y component. In the velocity power spectrum the washboard frequency peak narrows indicating greater temporal coherence, and higher harmonics become more visible. (d) As the density is increased to $\rho = 100/A = 0.00385/b_0^2$ the structure becomes more fully ordered into a triangular array, and the washboard peak sharpens.

widths at half maximum of the fundamental peaks, while the uncertainties for the calculated values are obtained from the standard deviations of the average velocities.

3.2.1 Randomly Distributed Columnar Defects

Noise characteristics and structure. Results for flux lines of different densities interacting with random columnar defects are displayed in Fig. 3.3. With the average spacing between defects set to $15\,b_0$ the number of columns in a unit area $A = 150\frac{2}{\sqrt{3}}\,b_0 \times 150\,b_0$ is 115. For a flux density $\rho = 16/A$ (a filling fraction of $\sim 1/7$) only broadband noise is observed in the velocity power spectrum, see Fig. 3.3(a). The corresponding diffraction pattern shows a ring indicating an isotropic liquid or amorphous solid. A typical Delaunay triangulation for the vortex positions in a snapshot of a particular run with 16 lines is depicted in Fig. 3.4(a). The plot shows the presence of a number of topological defects in the vortex system. The 'time exposure' plot in Fig. 3.4(c) of the flux line center-of-mass positions produces trajectories reminiscent of the 'braided rivers' observed in two-dimensional plastic flow simulations [29]. The trajectories appear to move and cross within winding channels. For a density $\rho = 36/A$ the two peaks located perpendicular to the drive direction fully

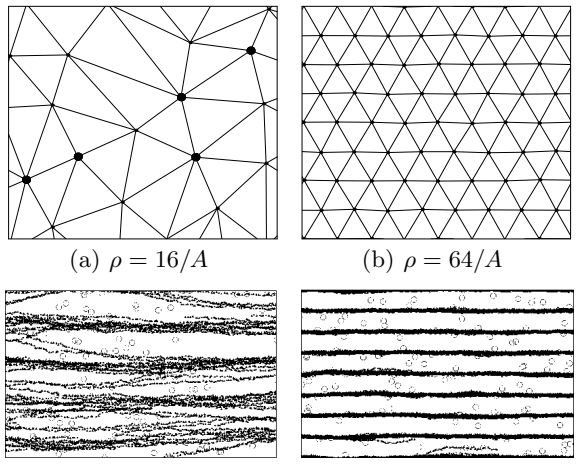

(a) $\rho = 16/A$ (b) $\rho = 64/A$

(c) $\rho = 16/A$ (d) $\rho = 64/A$

Fig. 3.4. Delaunay triangulation plots for the positions of (a) 16 and (b) 64 flux lines per area A in the presence of random columnar defects. Topological defects are marked. A disordered structure is obtained for flux density $\rho = 16/A$, while a triangular array free of topological defects is found for $\rho = 64/A$. A 'time exposure' for densities $16/A$ and $64/A$ is plotted in (c) and (d) to illustrate the flux line motion. Open circles indicate columnar defect locations, while black lines trace the trajectories of the average position of each vortex. For $\rho = 16/A$, the vortex trajectories cross suggestive of plastic flow, while for $\rho = 64/A$ parallel channels form.

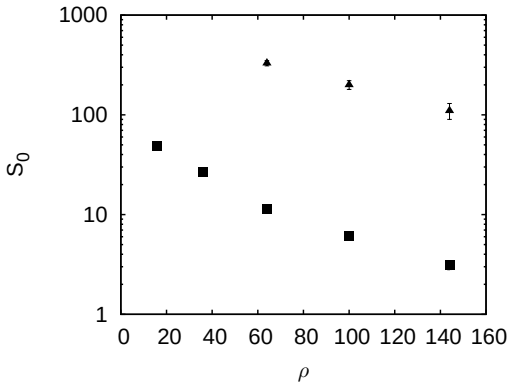

Fig. 3.5. Washboard peak power for increasing vortex density for columnar (square data points) and point defects (triangles). In either case the peak intensity is observed to decrease as the flux density is increased.

emerge, suggestive of the predicted moving transverse glass, see Fig. 3.3(b). Small intensity peaks with wave vector components parallel to the drive are also visible.

As the vortex density ρ is increased to $64/A$, peaks with an x component in the diffraction plot emerge more prominently and sharpen as shown in Fig. 3.3(c). Just as for $\rho = 36/A$, these peaks are smaller than those located perpendicular to the direction of the drive. In a typical associated Delaunay plot, Fig. 3.4(b), topological defects in the vortex lattice disappear, and the flux line trajectories form parallel channels, running in comparatively straight lines, Fig. 3.4(d). At $\rho = 100/A$ the structure plot reveals a well-ordered lattice of flux lines, see Fig. 3.3(d).

These results are a good demonstration of the competing energy scales in the system. The spatially randomly distributed pinning sites favor disordered flux line structures while the vortex repulsion induces ordering into a regular array. For $\rho = 16/A$ the structure factor displays a random vortex configuration, indicating that the lattice structure is dominated by the columnar pinning sites; indeed, the system is close to the depinning threshold, see Fig. 3.1(c). Individual vortices are pinned for periods of time that are long compared to the time it would take for the flux lattice to move one lattice constant, thus preventing the formation of the regular structure. At density $36/A$, the system has moved away from the depinning threshold, and the repulsive forces begin to separate the vortices into parallel channels resulting in spatial periodicity in the y direction (perpendicular to the drive), and by reaching $\rho = 64/A$ the system of moving vortices is dominated by the repulsive vortex interaction potential. At this stage individual channels begin to couple as additional periodicity appears in the x (drive) direction. Distinct peaks emerge in the diffraction plot with the peaks possessing a wave vector component in the x direction smaller than those with only a y component due to weaker coupling. As the density is increased to $\rho = 100/A$ the repulsive energy between the vortices grows further leading to a stronger coupling between transverse channels and eventually a symmetric triangular lattice structure emerges.

The spatial structure of the vortex array is reflected in the associated velocity or voltage power spectrum. At $\rho = 16/A$ a broadband signal is visible corresponding to the isotropic vortex distribution and their consequent random incoherent motion shown in Fig. 3.4(c). Similar broadband noise that is associated with incoherent flux transport has been experimentally and numerically observed in a number of studies [29,6,19]. For $\rho = 36/A$, as the vortices begin to arrange into a lattice a narrowband peak appears corresponding to the x wave vector components that appear in the structure factor plot. At a density $64/A$ the washboard signal narrows as the vortex system becomes more structured. A sharper peak indicates a greater temporal coherence between the vortices which is not surprising; as the density of the vortices is increased each vortex is more tightly held in its place and each line 'stiffened' by the repulsive forces exerted by its neighbors. For similar reasons the remnants of the broadband noise flatten out more. This trend continues as the flux density is further increased to $100/A$. As

the density is increased from $\rho = 64/A$ upward we observe a decrease in the washboard peak power, as shown in Fig. 3.5. The decrease of the fundamental peak intensity is due to the increase in stiffness of the lattice structure with growing vortex density. As each flux line passes through a defect site it will be less affected by the pin in a denser system resulting in smaller velocity fluctuations and hence reduced power output.

Washboard peak harmonics. In Table 3.1 the ratio of the intensities of the first and second harmonic with respect to the fundamental peaks are recorded for the velocity noise measured in the x and y directions. These ratios vary as the flux density increases indicating a change in the shape of the velocity vs. time trace. It is observed that the ratios approach values similar to those measured for point defects (listed in Table 3.2 below). We will investigate the relationship between the underlying defect type and the harmonics ratios in Sec. 3.3.1. A narrowband signal is also measured in the y direction transverse to the drive for densities of $64/A$ through $144/A$ flux lines (not shown). The ratios of the harmonics to the fundamental peak intensity in the y direction are also reported in Table 3.1. The frequency of the fundamental peak as well as the higher harmonics are identical to the frequencies measured in the x direction. While the power is lower in the y direction (by factors of 10 to 40), the ratios of the peak intensities are similar. Since there is no drive in the y direction, these observations could perhaps be interpreted as a suppression of transverse motion occurring at the same frequency as the washboard motion. One likely explanation is that as a vortex becomes temporarily trapped in a pinning potential, fluctuations transverse to the motion are suppressed until the vortex departs from the pinning site, resulting in periodic behavior.

Radius of gyration. In order to obtain additional information about the three-dimensional shape of the elastic vortex lines moving through a sample with columnar defects, we have obtained radius of gyration data, averaged over vortices, time, and defect configurations. We interpret the radius of gyration as the distance the elastic line is stretched from its average (center-of-mass) position. The components of the radius of gyration in the x and y direction vs. flux density are plotted in Fig. 3.6(a). As the flux density is increased the radius of gyration decreases indicating that the vortex lines are straightened at higher densities due to the stronger repulsion exerted by their nearest neighbors. The data also display anisotropy in the flux line 'stretching'. The magnitude of the radius of gyration is markedly greater along the direction of the drive than perpendicular to it, with the x and y components approaching each other only at quite large densities. For dilute systems we would expect the competition between the drive and the pinning potential to result in flexible vortices depinning in sections, with some parts of the flux lines leaving the columnar pins via 'double-kink' and 'half-loop' saddle-point configurations [14]. In the presence of the drive the free flux line sections move forward and grow, stretching the vortex until it depins completely. Since there is no drive in the y direction, the y component of the radius of gyration is smaller; however, the same trend is observed with increasing density as with the x component. At high densities the vortices are stiffer due to a smaller vortex separation distance. Rather than stretching, depinning tends toward an 'all or nothing' process with the tightly packed vortex ensembles effectively becoming two-dimensional.

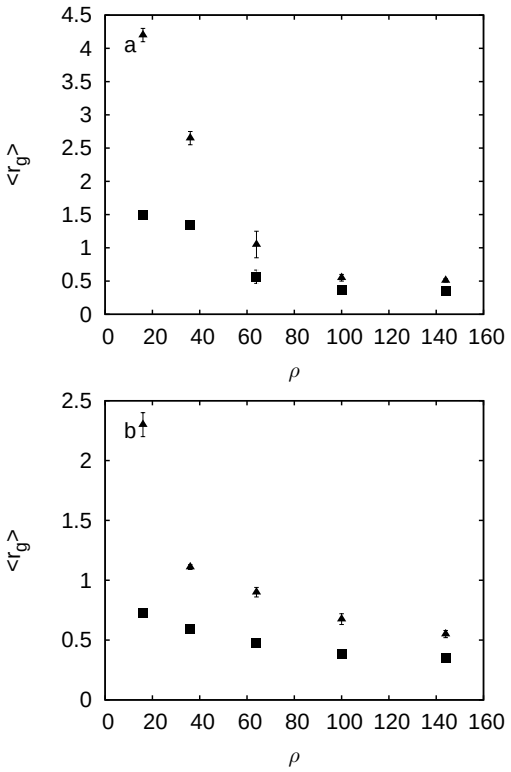

Fig. 3.6. Components of the mean radius of gyration for (a) columnar and (b) point pins. For both defect types the radius of gyration decreases with increasing vortex density. At higher flux densities vortices are caged by nearest neighbors, suppressing elastic flux line stretching. Lengths are reported in units of the pin radius b_0. ▲ - x component, ■ - y component.

Comparison with results obtained at small drive. The power spectra results reported above have been obtained at a rather high applied drive $f = 0.04$ chosen so that the washboard peak could be observed over a range of vortex densities. However, as discussed above, the velocity in the I-V characteristics (Fig. 3.1) begins to saturate at such high drive values, especially for systems with higher flux density. We believe that this is an artifact of the

Table 3.1. Ratio of the three largest peaks observed in the vortex velocity power spectrum in the presence of randomly distributed columnar defects. For each vortex density the ratios of the intensities of the second and third peak to the first are reported, for measurements taken in both the x and y directions. The number of runs over which the power spectral density plots were averaged is also listed. The corresponding power spectra peak ratios for a periodic piecewise linear (sawtooth) signal is included for comparison.

vortex density ρ	runs	ratio (x direction)	ratio (y direction)
$64/A = 0.00246/b_0^2$	115	$1 : 0.20 \pm 0.02 : 0.030 \pm 0.003$	$1 : 0.25 \pm 0.03 : 0.079 \pm 0.009$
$100/A = 0.00385/b_0^2$	44	$1 : 0.31 \pm 0.04 : 0.055 \pm 0.008$	$1 : 0.30 \pm 0.05 : 0.070 \pm 0.010$
$144/A = 0.00554/b_0^2$	44	$1 : 0.38 \pm 0.08 : 0.120 \pm 0.030$	$1 : 0.36 \pm 0.06 : 0.055 \pm 0.008$
$f(x) = x$, $0 < x < 2\pi$		$1 : 0.25 : 0.11$	

limited step size in the simulation. In order to investigate whether the velocity saturation influences the velocity fluctuations we now examine the power spectra at a lower drive value $f = 0.01$ and compare the results to those for $f = 0.04$. We consider here a dense vortex system with $\rho = 144/A$ subject to randomly placed columnar defects. This flux density was chosen to preserve the washboard peak at a lower drive. Results are displayed in Fig. 3.7. These data suggest that the velocity saturation does *not* adversely affect the velocity power spectra. The expected drop in washboard frequency corresponding to the decrease in applied drive is observed. The full peak widths at half maximum of the fundamental are measured at high and low drive and the results are found to be comparable (0.00036 rad/MCS and 0.00041 rad/MCS, respectively) indicating that the temporal correlations are not affected by the saturation. Both spectra display a similar harmonic ratio $1 : 0.40 \pm 0.05 : 0.10 \pm 0.01$. Likewise the structure factors are found to be similar. These results suggest that data obtained at high drive values do not possess any pronounced artifacts due to velocity saturation.

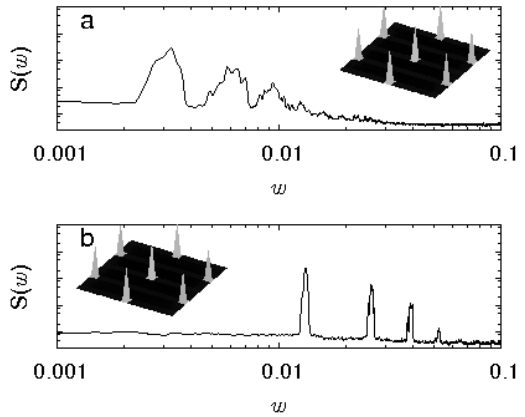

Fig. 3.7. Voltage power spectra for (a) low ($f = 0.01$) and (b) high ($f = 0.04$) driving forces at $\rho = 144/A$ in the presence of columnar defects.

3.2.2 Randomly Placed Point Defects

The results for the velocity power spectra and associated structure factors for vortices driven through randomly distributed point defects show many qualitative similarities to those obtained for columnar pins, see Fig. 3.8. However, the structure factor plot associated with an isotropic liquid is never observed in our simulations, even at the lowest flux densities. The intensities of the structure factor peaks increase with growing flux density, indicating an increasing degree of positional order in the system. For the lowest density system, Fig. 3.8(a), the structure factor plot implies greater spatial periodicity perpendicular to the direction of the drive than parallel to it, similar to the case of columnar defects, suggesting that parallel channels are not well-coupled in this regime. This is further evident in the Delaunay triangulation plot shown in Fig. 3.9(a). Compared to the system with a density $16/A$, the Delaunay plot for $\rho = 36/A$, Fig. 3.9(b), yields greater alignment perpendicular to the drive owing to the disappearance of topological defects in the vortex lattice. The reason for this is similar to that for columnar defects; the pinning sites introduce shear between parallel channels resulting in less-ordered rows of vortices that run perpendicular to the drive. As the density increases the vortex repulsion becomes the dominant energy in the system, and the coupling between parallel channels is enhanced.

In the velocity power spectrum for flux density $\rho = 16/A$ depicted in Fig. 3.8(a), the narrowband signal rests on a low broadband background signal. As the vortex density increases the broadband component diminishes, as do the power and width of the washboard peak. In general, the peak widths are smaller than those observed for columnar defects, as to be expected for uncorrelated and less efficient pinning centers. In the spectra where peaks are resolvable, the fundamental peak and higher harmonics are located at frequencies that are identical in the x and y directions. The ratio of the fundamental to the harmonics in either direction are listed in Table 3.2. These ratios for flux densities $\rho = 16/A$ through $100/A$ lines are comparable suggesting a similar shape of the velocity-time traces. For a sys-

Table 3.2. Ratio of the three largest washboard peaks observed in the velocity power spectrum for point defects. For each vortex density the ratios of the intensities of the second and third peak to the first are reported, for measurements taken in both x and y directions. The number of runs over which the power spectral density plots were averaged is also included.

vortex density ρ	runs	ratio (x direction)	ratio (y direction)
$16/A = 0.00062/b_0^2$	44	$1 : 0.67 \pm 0.09 : 0.27 \pm 0.02$	n / a
$36/A = 0.00139/b_0^2$	44	$1 : 0.55 \pm 0.06 : 0.22 \pm 0.02$	$1 : 0.4 \pm 0.1 : 0.40 \pm 0.10$
$64/A = 0.00246/b_0^2$	276	$1 : 0.58 \pm 0.03 : 0.24 \pm 0.01$	$1 : 0.51 \pm 0.04 : 0.16 \pm 0.01$
$100/A = 0.00385/b_0^2$	88	$1 : 0.56 \pm 0.05 : 0.25 \pm 0.02$	n / a
$144/A = 0.00554/b_0^2$	88	$1 : 0.80 \pm 0.10 : 0.19 \pm 0.02$	$1 : 0.43 \pm 0.06 : 0.08 \pm 0.01$

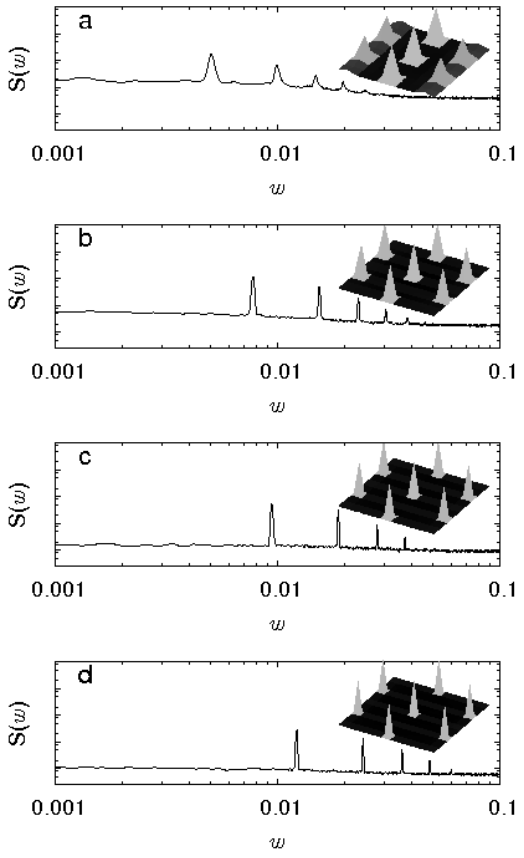

Fig. 3.8. Power spectra and structure factor plots for increasing vortex density ρ in the presence of point pins, with (a) $\rho = 16/A = 0.00062/b_0^2$, (b) $36/A = 0.00139/b_0^2$, (c) $64/A = 0.00246/b_0^2$, and (d) $100/A = 0.00385/b_0^2$. Narrowband washboard noise peaks are observed in all thespectral density plots, and six-fold coordination in the corresponding vortex structure factors.

tem with $\rho = 144/A$ the ratio is however markedly different. At this point it is not clear to us which physical mechanism dictates the detailed values of these peak intensity ratios. Yet, as we shall further argue in Sec. 3.3.1 below, we believe that these ratios characterize the overall deformation of the vortex lattice rather than reflect the geometry of the pinning centers.

The mean flux line radius of gyration (averaged over vortices, time, and pinning site distributions) vs. vortex density for point defects is plotted in Fig. 3.6(b). The behavior for both components is similar to that of a system subject to randomly placed columnar defects. A larger radius of gyration is observed for low-density systems, while it decreases for both x and y components as the flux density is increased. Unlike for columnar defects, the pinning force for uncorrelated point disorder does not add coherently over the length of the flux lines. Whereas the random spatial distribution of point pins promotes thermal flux line wandering, the stretching of the vortices while moving through a defect is not as severe. Comparing the data to those for columnar defects with identical flux densities, we note that the magnitudes of both components of the radius of gyration are smaller for point defects. As the density is increased both components of the radius of gyration for point defects approach the same values as also seen in the corresponding curves for columnar defects.

We have also examined the effect of the total vortex length L_z on the velocity power spectrum. Data for $L_z = 60$ (three times the length of the vortices shown in all previous results) at a density of 64 lines have been included in Figs. 3.10(a) and 3.10(b). (The peak power for $L_z = 20$ in normalized units is $1.14 \cdot 10^{-6} \pm 9 \cdot 10^{-8}$ compared to $4.2 \cdot 10^{-7} \pm 3 \cdot 10^{-8}$ for $L_z = 60$.) Qualitatively, the findings are quite similar to those for a shorter vortex length;

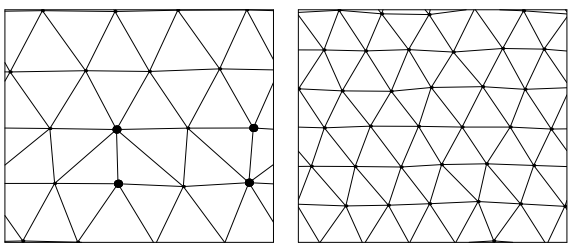

(a) $\rho = 16/A$ (b) $\rho = 36/A$

Fig. 3.9. Delaunay triangulation for vortices with densities (a) $\rho = 16/A$ and (b) $36/A$, interacting with randomly distributed point pinning centers. Topological defects are indicated.

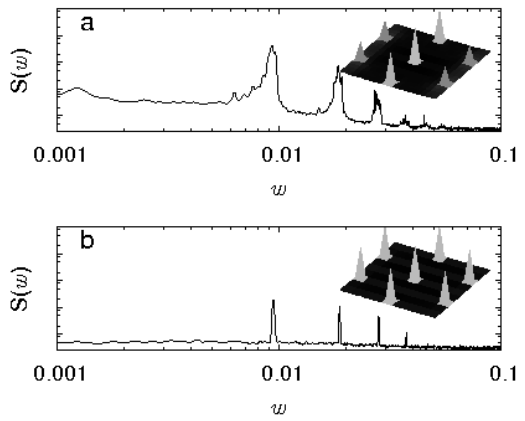

Fig. 3.10. Velocity fluctuation power spectra and structure factor plots for a flux density $\rho = 64/A$ for (a) columnar and (b) point defects in a spatially extended system with $L_z = 60$, i.e., all flux lines have been lengthened by a factor of 3 compared to the previous runs. The results for columnar defects shown in (a) are very similar to those for the same density with shorter lines, as depicted in Fig. 3.3(c). On the other hand, for point defects (b) the power drops noticeably compared to Fig. 3.8(c).

however, in the presence of point defects, compared to the results shown in Fig. 3.8(c), the narrowband power is lower. On the other hand, a similar intensity drop is not observed in the case of columnar defects, compare Fig. 3.10(a) to Fig. 3.3(c). The additional flux line length and the lack of spatial correlation in the z direction for point disorder further demonstrates the difference in pinning efficiency between point and columnar defects. For columnar pins the lengths of both the defect and the vortex span the height of the sample just as they did for the shorter system; hence we observe a similar effect on the motion and the power spectrum. For point defects, as the length of the vortex is increased the effect of a single point defect on the longer vortex decreases as a whole resulting in a smaller power output: local fluctuations are averaged out. We note that naturally these distinctions are only observable in three-dimension simulations.

3.3 Variable Pinning Efficiency

In this section we examine the effect of varying pinning efficiency on the vortex structure factor and velocity fluctuation power spectrum. We shall study the cases of different point pin strenghts and linear defects of fixed strength but varying length, thus interpolating between uncorrelated point disorder and correlated columnar defects. We are particularly interested in whether point and columnar defects display different washboard harmonic signatures in the velocity power spectrum.

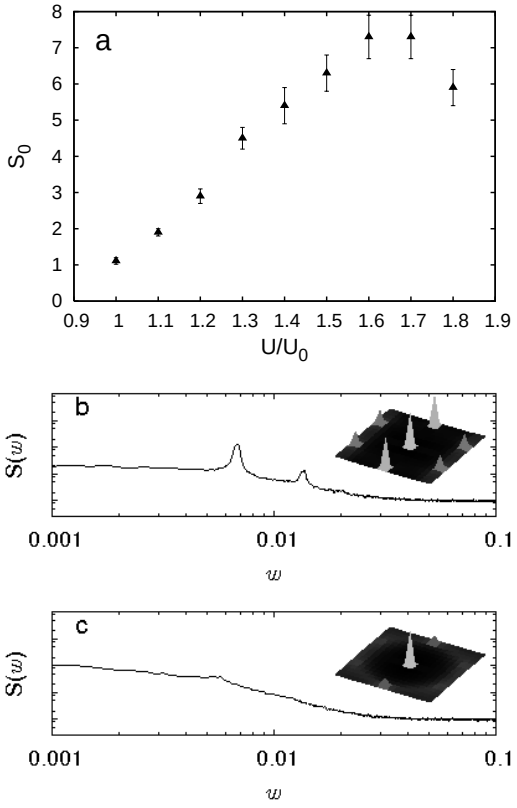

Fig. 3.11. (a) Velocity spectrum washboard peak power for increasing point pinning strength U. The vortex density is held constant at $\rho = 64/A$. As the pinning strength is increased the washboard signal grows to a maximum value around $1.7\,U_0$ (b) and then decreases as the system transitions to a broadband signal around $1.9\,U_0$ (c).

3.3.1 Variable Point Pinning Strength

To carry out this investigation simulation runs were performed at fixed flux density $\rho = 64/A$ while the point pinning strength was increased from the value U_0 used before up to $U = 1.9\,U_0$. For each pinning strength results were obtained by averaging over random distributions of point defects. The number of pinning sites per run was held constant; only the pinning strength was changed. The power of the washboard peak is plotted versus pinning strength in Fig. 3.11(a). We note that the power reaches a maximum value at approximately $1.7\,U_0$, see Fig. 3.11(b). The increase in power is due to the stronger pinning causing larger velocity fluctuations in the vortex array. The width of the peak increases along with its power as indicated by the error bars in Fig. 3.11(a). The signal then decreases as the power output transitions to a broadband signal coinciding with decreasing coherent vortex motion, Fig. 3.11(c).

Washboard harmonic peak ratios for a few pinning strenghts are recorded in Table 3.3. We com-

Table 3.3. Intensity ratio of the three largest velocity power spectrum peaks for increasing point defect pinning strength, recorded as multiples of the initial pinning strength U_0. For each pinning strength the ratios of the intensities of the first and second peak to the third are given for measurements taken in the drive (x) direction. The number of runs over which the power spectral density plots were averaged is also included.

U/U_0	runs	ratio (x direction)
1.1	44	$1 : 0.55 \pm 0.06 : 0.150 \pm 0.020$
1.3	44	$1 : 0.33 \pm 0.04 : 0.045 \pm 0.008$
1.5	44	$1 : 0.20 \pm 0.03 : 0.012 \pm 0.004$

pare these results to the columnar defect data in Table 3.1 and note that similar harmonic ratios are observed for the weaker columnar defects at a density of $\rho = 64/A$ and the stronger point defects with $U = 1.5\,U_0$. These findings demonstrate that the harmonic ratios are not unique signatures of the material defect types compared in this study. We speculate that the ratios are rather dependent on the amount of deformation of the vortex lattice by the defects regardless of whether or not the pins extend along the length of the vortices.

3.3.2 Variable Linear Defect Length

To further compare the effects of point and columnar defects on the velocity power spectrum, we have investigated systems with varying columnar defect lengths at a constant vortex density $\rho = 16/A$. Each set of results is obtained by averaging runs over random distributions of linear defects of a particular length l, with the total number of pinning sites held constant. Defect lengths vary from a single pinning site, i.e., random point defects, to a length of 10 contiguous pinning sites. (Recall that a columnar defect extending over 20 pinning sites spans the entire system height $L_z = 20$.) The driving force remains at $f = 0.04$. As the defect length is increased the spatial order in the system decreases as indicated by the structure factor peaks in Fig. 3.12. Peaks with wave vector components along the drive decrease in intensity at shorter defect lengths compared to those perpendicular to the drive. With increasing length of the linear pins (growing defect correlations) the peak intensities become diminished. Results for defect length $l = 1$, 3, and 5 are shown in Fig. 3.12. By length $l = 10$ the washboard peak disappears entirely and is replaced by a broadband signal (not shown). We note a second peak with a frequency corresponding to the system size also appears in the power spectrum $l = 3$. While the cause of this peak is unclear, one possible explanation is that it originates in some type of persistent deformation in the vortex lattice. With periodic boundary conditions this lattice deformation

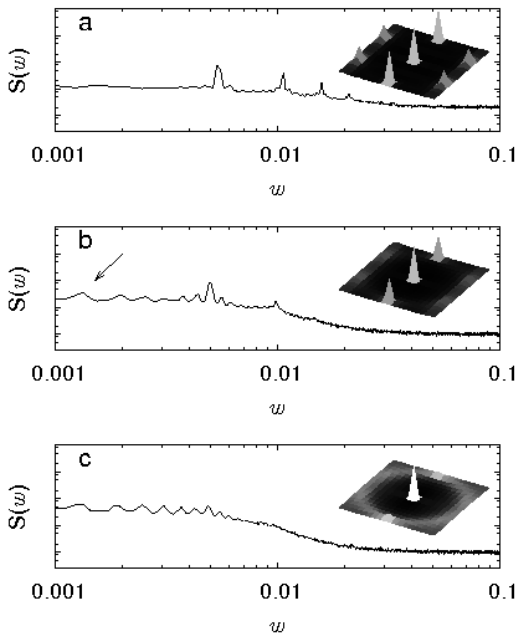

Fig. 3.12. Vortex velocity / voltage power spectra and diffraction plots for increasing columnar defect lengths at a fixed vortex density $\rho = 16/A = 0.00062/b_0^2$ with (a) $l = 1$, (b) $l = 3$, and (c) $l = 5$. The results reveal how the system evolves from an ordered to a disordered configuration as the defect length increases. The washboard signal decreases as the broadband noise grows.

would repeatedly travel over the same pinning distribution resulting in a periodicity corresponding to the 'time of flight' across the system. As a comparison runs were performed for various point defect pinning strengths at the same low flux density $\rho = 16/A$. The process was identical to the previous section. However, due to the lower density, when the depth of the pinning potential well was increased to only 1.5 times its original value U_0, the washboard peak completely disappeared. The results of these simulations are shown in Fig. 3.13. We observe that these results look quite similar to those from increasing the linear defect lengths.

While the above power spectra are qualitatively comparable, the growth of the mean vortex line radius of gyration turns out to be quantitatively different in both situations, as shown in Fig. 3.14. The data for columnar disorder initially grows as an exponential function, $r_g \propto \exp(-l_0/l)$ where l is the length of the columnar defects, while the data for point defects is best described by a quadratic fit $r_g \propto (U/U_0)^2$. While we cannot offer a quantitative theory for these trends, they can be understood qualitatively by examining the average vortex velocity as these two pinning types are varied. For both cases as the 'pinning effectiveness' is increased the velocity decreases and the radius of gyration increases. We interpret the increase in radius of gy-

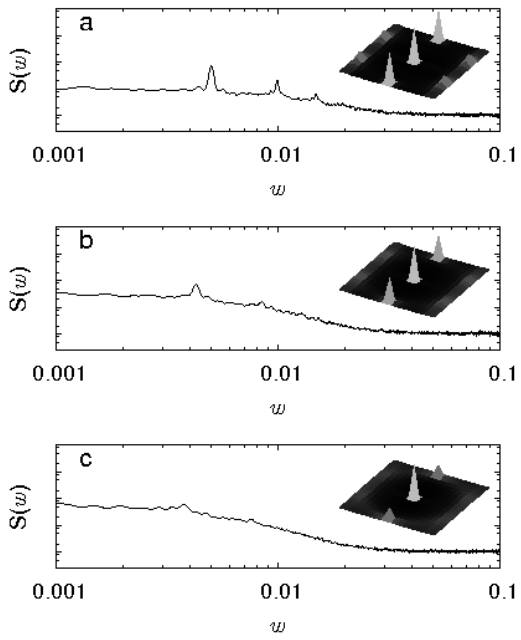

Fig. 3.13. Results for simulations with random point defects whose pinning strength is increased from its original value U_0 in (a) to (b) $U = 1.2\,U_0$ and $U = 1.4\,U_0$ at a low vortex density $\rho = 16/A = 0.00062/b_0^2$.

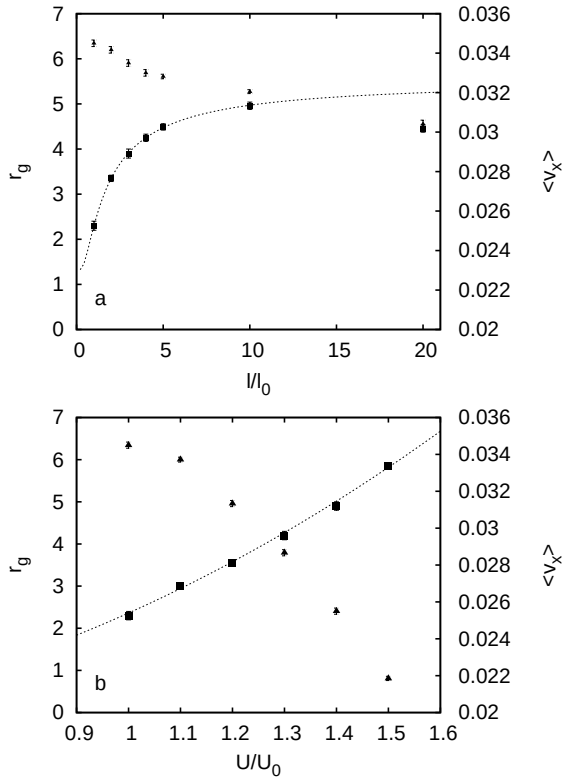

Fig. 3.14. Mean flux line radius of gyration and average velocity for (a) increasing linear defect length and (b) enhanced point pinning strength. The radius of gyration data for increasing lengths initially follows an exponential of the form $r_g \propto \exp(-l_0/l)$ while the data for increasing pinning strength is best described by a quadratic fit. ▲ - average velocity, ■ - radius of gyration (x component).

ration as the vortices being stretched as they are simultaneously held by the defects and pulled by the externally applied drive. As the linear defect length is increased the velocity decreases, but by length $l = 20$ (the height of the system) the vortices are still moving. [Compare the velocity trends in Fig. 3.14(a) and (b).] This indicates that the columnar defects cannot stop the vortices at this particular flux density and applied drive, and the 'stretching' of the vortices is limited leading to saturation of the radius of gyration. On the other hand, for the point pins the pinning strength is not limited leading to greater stretching.

4 Summary and Conclusion

To summarize, a non-equilibrium Monte Carlo simulation code has been developed to study the effects of different types of pinning centers on the velocity power spectrum of vortices driven through a disordered medium in the non-equilibrium steady state [23,24]. Specifically, we have investigated the evolution of the washboard signal as we have increased the vortex / magnetic flux density in the presence of point and columnar defects. In order to achieve a more complete understanding of the velocity power spectra, we have also examined the corresponding two-dimensional vortex structure factor and the average flux line radius of gyration.

We have confirmed that our numerical model displays the appropriate physical behavior over a large section of parameter space. For instance, vortices arrange into a six-fold lattice when interacting with only weak material defects. In the presence of an applied current and sufficiently strong pinning sites, the vortex lattice reorients with a lattice vector along the drive direction. Furthermore, we have obtained the current-voltage characteristics and found these to be qualitatively similar to I-V curves obtained in experiments. In our simulation vortices depin above a critical applied force and gain velocity as the applied force is increased. Changes in the I-V curves due to different pinning site types and vortex densities occur as expected.

At high applied drive, our algorithm produces saturating I-V curves, an artifact that originates in a necessary limitation of the maximum allowed displacements. However, we have provided evidence that suggests this limitation does not adversely affect the associated power spectra and other physical quantities in the regime investigated here.

Expected physical behavior is also observed in the vortex structure factor. For both pointlike and linear extended defects, as the vortex density is increased spatial ordering is observed to increase in the diffraction plots. When interacting with columnar pins, the vortex system structure factor is found to evolve from that of a liquid, to a smectic, and finally a triangular lattice. For point defects only the regular triangular array is realized in the parameter space studied here. We remark that the structure factor plots with point defects at low vortex densities appear qualitatively similar to those for columnar defects at higher flux densities.

Velocity fluctuation or voltage noise power spectra measured parallel to the drive have been obtained for various vortex densities in the presence of both columnar and point defects. A narrowband signal is observed over a large vortex density interval, with the peak coinciding with the washboard frequency. The power spectrum has also been measured perpendicular to the drive, and a signal at the washboard frequency is observed there as well. Harmonics have been detected at multiples of the washboard frequency for both types of disorder. For columnar defects the ratios of the power of the first and second harmonic to the third turn out to be larger than for point defects. However, as the density is increased, the ratio decreases for columnar defects. By varying the pinning strength of the point defects at a constant vortex density we have obtained similar harmonic ratios to that of columnar defects. This indicates that the harmonic ratios are not unique indicators of the type of material defects present in the sample. Rather, we think that the harmonic ratios should be a function of the degree of deformation of the vortex lattice. We remark that the detailed features of the flux flow power spectrum are also influenced by the configuration of the leads above the sample surface [2]. In real experimental setups, these effects may mask the noise signatures observed in our simulations.

In order to investigate the shape of the fluctuating vortex lines we have determined the average radius of gyration in the presence of point and columnar defects in the x and y directions. The general (and expected) trend is for the radius of gyration to decrease as the density of the vortices is increased. Our results for the gyration radius also reveal that transverse fluctuations do not appear to play a large role in the thermal flux line wandering for the range of parameters investigated here: The transverse component in fact rarely exceeds the radius of a pinning site except for the lowest vortex densities studied.

In addition, we have measured these various observables as the columnar defect length, i.e., the degree of correlation in the disorder was varied, and compared the results to the effects of varying just the pinning strength of point defects. Changing the defect character from point-like to columnar shows similar results to increasing point defect pinning strength in both the diffraction and power spectral density plots. Different effects on the vortices through adjusting these two distinct pinning mechanisms become apparent upon comparing the growth of the radius of gyration in the direction along the drive. While the results seem to correspond to physical intuition, a precise theory explaining the quantitative growth of the radius of gyration in either situation is currently lacking and will have to be developed.

This work was in part supported through the U.S. National Science Foundation, Division of Materials Research, grants NSF DMR-0075725 and 0308548, and through the Bank of America Jeffress Memorial Trust, research grant J-594. Some of the data shown were obtained from simulations run on Virginia Tech's Anantham cluster. We gratefully acknowledge helpful discussions with I. Georgiev, T. Klongcheongsan, E. Lyman, M. Pleimling, G. Pruessner, B. Schmittmann, S. Teitel, and R.K.P. Zia.

References

1. For a detailed review, see: G. Blatter, M. V. Feigel'man, V. B. Geshkenbein, A. I. Larkin, and V. M. Vinokur, Rev. Mod. Phys. **66** 1125 (1994).
2. J. R. Clem, Phys. Rep. **75**, 1 (1981).
3. E. H. Brandt, Phys. Rev. Lett. **50**, 1599 (1983).
4. T. Matsuda, K. Harada, H. Kasai, O. Kamimura, and A. Tonomura, Science **271**, 1393 (1996).
5. H. J. Jensen, A. Brass, and A. J. Berlinsky, Phys. Rev. Lett. **60**, 1676 (1988).
6. A. Vestergren and M. Wallin, Phys. Rev. B **69**, 144522 (2004).
7. U. Yaron, P. L. Gammel, D. A. Huse, R. N. Kleiman, C. S. Oglesby, E. Bucher, B. Batlogg, D. J. Bishop, K. Mortensen, K. Clausen, C. A. Bolle, and F. De La Cruz, Phys. Rev. Lett. **73**, 2748 (1994).
8. A. E. Koshelev and V. M. Vinokur, Phys. Rev. Lett. **73**, 3580 (1994).
9. T. Giamarchi and P. Le Doussal, Phys. Rev. Lett. **76**, 3408 (1996); P. Le Doussal and T. Giamarchi, Phys. Rev. B **57**, 11356 (1998).
10. V. Gotcheva, A.T.J. Wang, and S. Teitel, Phys. Rev. Lett. 92, 247005 (2004); V. Gotcheva, Y. Wang, A. T. J. Wang, and S. Teitel, Phys. Rev. B **72**, 064505 (2005).
11. Q.-H. Chen and X. Hu, Phys. Rev. Lett. **90**, 117005 (2003).
12. G. Grüner, Rev. Mod. Phys. **60**, 1129 (1988); *Density Waves in Solids* (Addison-Wesley, Reading, MA 1994).
13. L. Civale, A. D. Marwick, T. K. Worthington, M. A. Kirk, J.R. Thompson, L. Krusin-Elbaum, Y. Sun, J. R. Clem, and F. Holtzberg, Phys. Rev. Lett. **67**, 648 (1991).

14. D. R. Nelson and V. M. Vinokur, Phys. Rev. Lett. **68**, 2398 (1992); Phys. Rev. B **48**, 13060 (1993).
15. E. Olive, J. C. Soret, P. Le Doussal, and T. Giamarchi, Phys. Rev. Lett. **91**, 037005 (2003).
16. A. T. Fiory, Phys. Rev. Lett. **27**, 501 (1971).
17. J. M. Harris, N. P. Ong, R. Gagnon, and L. Taillefer, Phys. Rev. Lett. **74**, 3684 (1995).
18. A. M. Troyanovski, J. Aarts, and P. H. Kes, Nature (London) **399**, 665 (1999).
19. Y. Togawa, R. Abiru, K. Iwaya, H. Kitano, and A. Maeda, Phys. Rev. Lett. **85**, 3716 (2000).
20. C. J. Olson, C. Reichhardt, and F. Nori, Phys. Rev. Lett. **81**, 3757 (1998).
21. A. B. Kolton, D. Domńguez, and N. Gronbech-Jensen, Phys. Rev. B **65**, 184508 (2002).
22. H. Fangohr, S. J. Cox, and P. A. J. de Groot, Phys. Rev. B **64**, 064505 (2001).
23. T. J. Bullard, Ph. D. Thesis, Virginia Polytechnic Institute and State University (2005).
24. J. Das, T. J. Bullard, and U. C. Täuber, Physica A **318**, 48 (2003).
25. A. Rosso and W. Krauth, Phys. Rev. B **65**, 012202 (2001).
26. P. Sen, N. Trivedi, and D. M. Ceperley, Phys. Rev. Lett. **86**, 4092 (2001).
27. We observe that with a severe cut-off the system becomes locked into a particular spatial configuration, as each line is effectively caged within the deep potential energy minima formed by linear superposition of its neighbors' step-function potentials.
28. S. Katz, J. L. Lebowitz, and H. Spohn, Phys. Rev. B **28** 1655 (1983).
29. C. J. Olson, C. Reichhardt, and F. Nori, Phys. Rev. Lett. **80**, 2197 (1998).
30. W. H. Kleiner, L. M. Roth, and S. H. Autler, Phys. Rev. **133**, A1226 (1964).
31. A. Schmid and W. Hauger, J. Low Temp. Phys. **11**, 667 (1973).
32. Y. Ando, N. Motohira, K. Kitazawa, J.I. Takeya, and S. Akita, Phys. Rev. Lett. **67**, 2737 (1991).
33. L. Ammor, B. Pignon, and A. Ruyter, Phys. Rev. B **69**, 134508 (2004).
34. Q. Li, H. J. Wiesmann, M. Suenaga, L. Motowidlow, and P. Haldar, Phys. Rev. B **50**, 4256 (1994).
35. C. J. Olson, G. T. Zimányi, A. B. Kolton, and N. Gronbech-Jensen, Phys. Rev. Lett. **85**, 5416 (2000).
36. A. B. Kolton, D. Domínguez, C. J. Olson, and N. Gronbech-Jensen, Phys. Rev. B **62**, R14 657 (2000).

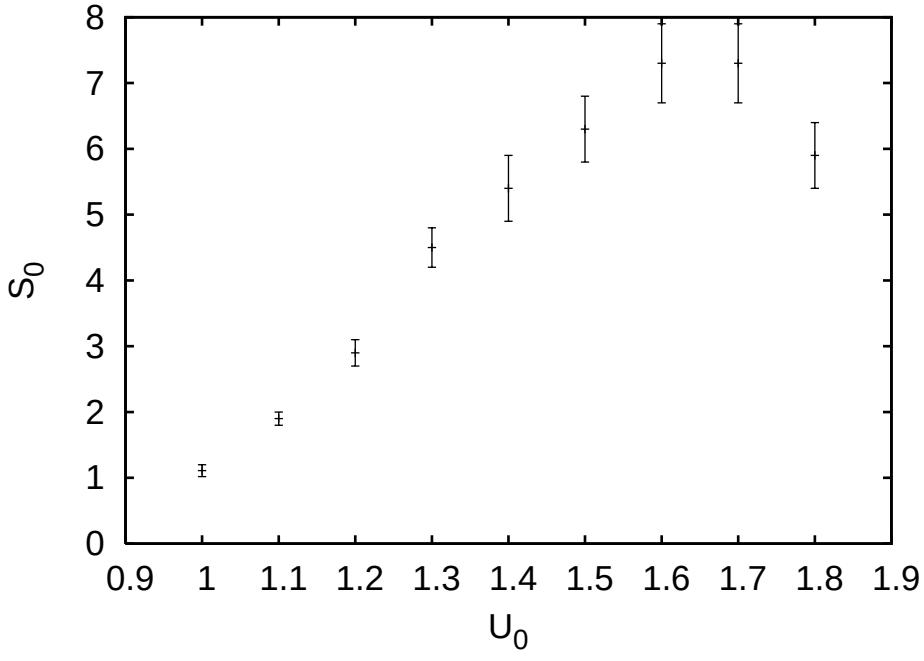
8
7
6
5
4
3
2
1
0
S_0
0.9
1
1.1
1.2
1.3
1.4
1.5
1.6
1.7
1.8
1.9
U_0

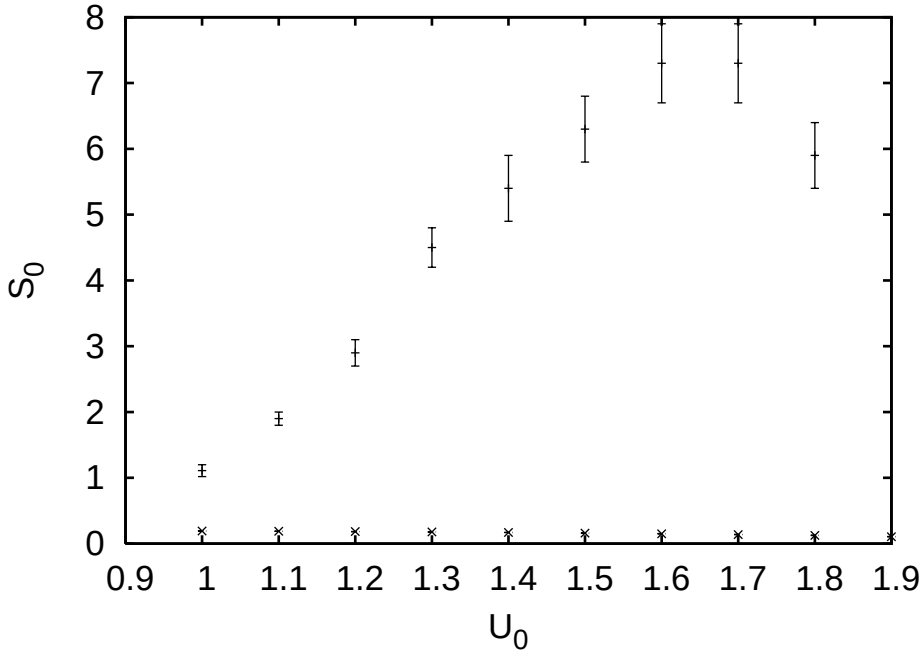
8
7
6
5
4
3
2
1
0
S_0
0.9
1
1.1
1.2
1.3
1.4
1.5
1.6
1.7
1.8
1.9
U_0